Journal of Sound and Vibration (2002) **252**(2), 261–280
doi:10.1006/jsvi.2001.3877, available online at http://www.idealibrary.com on IDEAL®

EFFECT OF DYNAMIC ROLLING OSCILLATIONS ON TWIN-TAIL BUFFET RESPONSE

E. F. Sheta† and O. A. Kandil

Department of Aerospace Engineering, Old Dominion University, Norfolk, VA 23529, *U.S.A.*
E-mail: efs@cfdrc.com

(*Received* 1 *November* 1999, *and in final form* 10 *May* 2001)

The effect of dynamic rolling oscillations of delta-wing/twin-tail configuration model on twin-tail buffet response is investigated. The configuration model is statically pitched at a 30° angle of attack and then forced to oscillate in roll around the symmetry axis at a constant amplitude of 4° and reduced frequency of π and 2π. This multidisciplinary problem is solved using three sets of equations on a dynamic multi-block grid structure. The first set is the unsteady, full Navier–Stokes equations, the second set is the aeroelastic equations for coupled bending and torsion vibrations of the tails, and the third set is the grid-displacement equations. The results conclusively showed that the rolling oscillations of the configuration have led to higher loads, higher deflections, and higher excitation peaks than those of the stationary configuration. Moreover, increasing the reduced frequency has led to higher loads and excitation peaks and lower bending and torsion deflections and acceleration. The unsteady aerodynamic loads have never reached complete periodicity due to the irregular vibrations of the left and right tails.

1. INTRODUCTION

In order to maximize the effectiveness of the fighter aircraft that operate well beyond the buffet onset boundary, the design of the new generation of fighter aircraft should account for both high maneuver capabilities at high and wide range of angles of attack, and the aeroelastic buffet characteristics at high alpha. The maneuver capabilities are achieved, for example in the F/A-18 fighter, through the combination of leading-edge extension (LEX) with a delta wing and the use of vertical tails. The LEX maintains lift at high angles of attack by generating a pair of vortices that trail aft over the top of the aircraft. The vortex entrains air over the vertical tails to maintain stability of the aircraft. At some flight conditions, the vortices emanating from the highly swept LEX of the delta wing break down before reaching the vertical tails which get bathed in a wake of unsteady highly turbulent, swirling flow. The vortex-breakdown flow produces unsteady, unbalanced loads on the vertical tails and causes a peak in the pressure spectrum that may be tuned to different structural modes depending on the angle of attack and dynamic pressure. This in turn produces severe buffet on the tails and has led to their premature fatigue failure. Therefore, the evaluation of the buffet characteristics must account for the turbulent characteristics of the oncoming flow. If the power spectrum of the turbulence is accurately predicted, the intensity of the buffeting motion can be computed and the structural components of the aircraft can be designed to alleviate the buffet response.

† Current address: CFD Research Corporation, 215 Wynn Drive, Huntsville, AL 35805, U.S.A.

0022-460X/02/$35.00

Experimental investigation of the vertical tail buffet of the F/A-18 models have been conducted by several investigators such as Sellers *et al.* [1], Erickson *et al.* [2], Wentz [3], Lee and Brown [4], and Cole *et al.* [5]. These experiments showed that the vortex produced by the LEX of the wing breaks down ahead of the vertical tails at angles of attack of 25° and higher producing unsteady loads on the vertical tails, and the buffet response occurs in the first bending mode, increases with increasing dynamic pressure and is larger at $M = 0{\cdot}3$ than that at higher Mach numbers.

An extensive experimental investigation has been conducted to study vortex–tail interaction on a 76° sharp-edged delta wing with vertical twin-tail configuration by Washburn *et al.* [6]. The vertical tails were placed at nine locations behind the wing. The experimental data showed that the aerodynamic loads are more sensitive to the chordwise tail location than its spanwise location. As the tails were moved laterally toward the vortex core, the buffeting response and excitation were reduced. Although the tail location did not affect the vortex-core trajectories, it affected the location of vortex-core breakdown. Moreover, the investigation showed that the presence of a flexible tail could affect the unsteady pressures on a rigid tail on the opposite side of the model.

Kandil *et al.* [7] presented the first successful computational simulation of the vertical-tail buffet using a delta wing-single flexible vertical-tail configuration. The tail was allowed to oscillate in bending modes. Unsteady vortex breakdown of leading-edge vortex cores was captured, and unsteady pressure forces were obtained on the tail. Kandil *et al.* [8–10] allowed the vertical tail to oscillate in both bending and torsional modes. The total deflections and the frequencies of deflections and loads of the coupled bending–torsion case were found to be one order of magnitude higher than those of the bending case only. The loads on the tail in the transonic flow regime were one order of magnitude lower than those of the subsonic flow. Also, it has been shown that the tail oscillations change the vortex breakdown locations and the unsteady aerodynamic loads on the wing and tail.

Kandil *et al.* [11, 12] studied the buffet response of generic fighter aircraft equipped with F/A-18 and a generic F-117 twin tails at $\alpha = 30°$ and for different spanwise locations of the twin tails. A multi-block grid structure was used to solve the problem. The loads, deflections, frequencies and root bending moments were reduced as the twin tails moved laterally toward the vortex core. The outboard location of the tails produced the least of these responses. In another paper by Kandil *et al.* [13], the buffet response of a twin-tail model in turbulent flow was considered at a wide range of angles of attack. The computational results were in good quantitative agreement with the experimental data of Washburn *et al.* [6]. In a recent paper by Sheta and Kandil [14], the effect of configuration pitching-up motion on twin-tail buffet response was investigated.

In this paper, the effect of configuration rolling oscillation on twin-tail buffet response is investigated. A dynamic multi-block grid structure is used to solve the problem for the inboard position of the twin tails. The configuration is forced to roll with a constant amplitude of 4° and reduced frequency of π and 2π. The computed results are compared with the results of stationary configuration.

2. FORMULATION

The formulation of the problem consists of three sets of governing equations along with certain initial and boundary conditions. The first set is the unsteady, compressible, full Navier–Stokes equations. The second set consists of the aeroelastic equations for bending and torsional vibrations of the tails. The third set consists of equations for moving the grid

according to the tail deflections and the rolling motions. Next, the governing equations of each set along with the initial and boundary conditions are given.

2.1. FLUID-DYNAMICS EQUATIONS

The conservative form of the dimensionless, unsteady, compressible, full Navier–Stokes equations in terms of time-dependent, body-conformed co-ordinates ξ', ξ^2, and ξ^3 is given by

$$\frac{\partial}{\partial t}\bar{Q} + \frac{\partial \bar{E}_m}{\partial \xi^m} - \frac{\partial (\bar{E}_v)_s}{\partial \xi^s} = 0, \quad m, s = 1, 2, 3, \tag{1}$$

where

$$\xi^m = \xi^m(x_1, x_2, x_3, t), \qquad \bar{Q} = \frac{1}{J}[\rho, \rho u_1, \rho u_2, \rho u_3, \rho e]^{\mathrm{T}}. \tag{2, 3}$$

$\bar{E}_m$ and $(\bar{E}_v)_s$ are the ξ^m-inviscid flux and ξ^s-viscous and heat conduction flux respectively. Details of these fluxes are given by Sheta [15].

2.2. AEROELASTIC EQUATIONS

The dimensionless, linearized governing equations for the coupled bending and torsional vibrations of a vertical tail that is treated as a cantilevered beam are considered. The tail bending and torsional deflections occur about an elastic axis that is displaced from the inertial axis. All the structural properties are free to vary in the vertical direction. All the displacements are assumed small and the cross-section of the beam is assumed to be rigid. These equations for the bending deflection, w, and the twist angle, θ, are given by

$$\frac{\partial^2}{\partial z^2}\left[EI(z)\frac{\partial^2}{\partial z^2}w(z, t)\right] + m(z)\frac{\partial^2}{\partial t^2}w(z, t) + m(z)x_\theta(z)\frac{\partial^2}{\partial t^2}\theta(z, t) = N(z, t), \tag{4}$$

$$\frac{\partial}{\partial z}\left[GJ(z)\frac{\partial}{\partial z}\theta(z, t)\right] - m(z)x_\theta(z)\frac{\partial^2}{\partial t^2}w(z, t) - I_\theta(z)\frac{\partial^2}{\partial t^2}\theta(z, t) = -M(z, t), \tag{5}$$

where z is the vertical distance from the tail-root fixed support. $EI(z)$ and $GJ(z)$ are the bending and torsional stiffness of the tail section. $m(z)$ is the mass per unit length, I_θ is the mass moment of inertia per unit length about the elastic axis, x_θ is the distance between the elastic axis and the inertia axis, N and M are the normal force and twisting moment per unit length. The centrifugal force components on the rotating tails are small because of the low reduced frequency of the rolling motion. Therefore, the centrifugal force is neglected in the aeroelastic equations. These components exert an important influence on rotary wing aircraft and turbomachinery where the reduced frequency is very high. The characteristic parameters for the dimensionless equations are c, a_∞, ρ_∞ and c/a_∞ for the length, speed, density and time, where c is the delta wing root-chord length, a_∞ the freestream speed of sound and ρ_∞ the freestream air density. The geometrical and natural boundary conditions on w and θ are given by

$$w(0, t) = \frac{\partial}{\partial z}w(0, t) = \frac{\partial^2}{\partial z^2}w(b, t) = \frac{\partial}{\partial z}\left[EI(b)\frac{\partial^2}{\partial z^2}w(b, t)\right] = 0, \tag{6}$$

$$\theta(0, t) = \frac{\partial}{\partial z}\theta(b, t) = 0. \tag{7}$$

The solution of equations (4) and (5) are assumed to be

$$w(z,t) = \sum_{i=1}^{k} \varphi_i(z) q_i(t), \qquad \theta(z,t) = \sum_{j=k+1}^{2k} \varphi_j(z) q_j(t), \tag{8,9}$$

where φ_i and φ_j are comparison functions satisfying the free-vibration modes of bending and torsion, respectively, and $q_i(t)$ and $q_j(t)$ are generalized time-dependent co-ordinate functions for bending and torsion, respectively, and k is the number of assumed modes for both bending and torsion. In this paper, the number of bending modes is six and the number of torsion modes is also six. Substituting equations (8) and (9) into equations (4) and (5) and using the Galerkin method along with integration by parts and applying the boundary conditions (equations (6) and (7)), we get the following equation for the generalized co-ordinates $q_i(t)$ and $q_j(t)$ in matrix form:

$$\underbrace{\begin{bmatrix} M_{11} & M_{12} \\ M_{21} & M_{22} \end{bmatrix}}_{\text{Mass matrix}} \begin{pmatrix} \ddot{q}_i \\ \ddot{q}_j \end{pmatrix} + \underbrace{\begin{bmatrix} K_{11} & 0 \\ 0 & K_{22} \end{bmatrix}}_{\text{Stiffness matrix}} \begin{pmatrix} q_i \\ q_j \end{pmatrix} = \underbrace{\begin{pmatrix} \hat{N}_i \\ \hat{N}_j \end{pmatrix}}_{\text{Aerodynamic load vectors}}, \qquad \begin{pmatrix} i = 1, 2, \ldots, k \\ j = k+1, \ldots, 2k \end{pmatrix}, \tag{10}$$

where

$$M_{11} = \int_0^h m\varphi_r\varphi_i \,\mathrm{d}z, \quad M_{12} = M_{21} = \int_0^h m x_\theta \varphi_r \varphi_j \,\mathrm{d}z, \quad M_{22} = \int_0^h I_\theta \varphi_s \varphi_j \,\mathrm{d}z,$$

$$K_{11} = \int_0^h EI \frac{\mathrm{d}^2\varphi_r}{\mathrm{d}z^2}\frac{\mathrm{d}^2\varphi_i}{\mathrm{d}z^2}\mathrm{d}z, \quad K_{22} = \int_0^h GJ \frac{\mathrm{d}\varphi_s}{\mathrm{d}z}\frac{\mathrm{d}\varphi_j}{\mathrm{d}z}\mathrm{d}z, \quad \hat{N}_i = \int_0^h \varphi_r N \,\mathrm{d}z, \quad \hat{N}_j = \int_0^h \varphi_s M \,\mathrm{d}z. \tag{11}$$

The numerical integration of equation (11) is obtained using the trapezoidal method with 125 points to improve the accuracy of integrations. The solution of equation (10), for $q_i(t)$; $i = 1, 2, \ldots, k$ and $q_j(t)$; $j = k+1, \ldots, 2k$ is obtained using the Runge–Kutta scheme. Next, w and θ are obtained from equations (8) and (9).

2.3. GRID DISPLACEMENT EQUATIONS

Once w and θ are obtained at the $n+1$ time step, the new grid co-ordinates are obtained using simple interpolation equations. In these equations, the twin-tail bending displacements, $w_{i,j,k}^{n+1}$, and their displacement through the torsion angle, $\theta_{i,j,k}^{n+1}$ are interpolated through cosine functions [15]. The motion of the grid points due to the rolling motion is taken into consideration using Euler angles of rotation. Once the new grid co-ordinates are defined, the metric and grid-speed terms are updated accordingly.

2.4. BOUNDARY AND INITIAL CONDITIONS

The boundary conditions consist of conditions for the fluid flow and conditions for the aeroelastic bending and torsional deflections of the twin tail. For the fluid flow, the Riemann-invariant boundary conditions are enforced at the inflow and outflow boundaries

of the computational domain. At the plane of geometric symmetry, periodic boundary conditions are specified. On the wing and tail surfaces, the no-slip and no-penetration conditions are enforced, that is the relative velocity must be equal to zero. The relative velocity is used here due to the dynamic motion of the wing and tail surfaces. The normal pressure gradient, $\partial p/\partial \hat{n}$, is equal to zero on stationary wing or tail surfaces. On the accelerating wing and tail, the normal pressure gradient is no longer equal to zero due to the acceleration of the grid points. The normal pressure gradient on dynamic bodies becomes $\partial p/\partial \hat{n} = -\rho \mathbf{a} \cdot \hat{n}$, where $\mathbf{a}$ is the acceleration of a point on the accelerating surface and $\hat{n}$ is the surface unit normal. The acceleration vector due to the coupled bending and torsion deflections of the tail is given by

$$\mathbf{a} = -\mathbf{r}\left[\frac{\partial^2\theta}{\partial t^2}\sin\theta + \left(\frac{\partial\theta}{\partial t}\right)^2\cos\theta\right]\hat{i} + \left\{\frac{\partial^2 w}{\partial t^2} + \mathbf{r}\left[\frac{\partial^2\theta}{\partial t^2}\cos\theta - \left(\frac{\partial\theta}{\partial t}\right)^2\sin\theta\right]\right\}\hat{j}, \quad (12)$$

where $\mathbf{r}$ is the vector distance to a specific point from the elastic axis of the tail. The acceleration vector due to rigid-body dynamics of the wing/twin-tail configuration is given by

$$\mathbf{a} = \dot{\mathbf{\Omega}} \times \mathbf{r} + \mathbf{\Omega} \times (\mathbf{\Omega} \times \mathbf{r}), \quad (13)$$

where $\mathbf{r}$ is the vector distance to the specific point from the pivot axis, and $\mathbf{\Omega}$ and $\dot{\mathbf{\Omega}}$ are the angular velocity and angular accelerations vectors of the forced rolling motion respectively.

The initial conditions consist of conditions for the fluid flow and conditions for the aeroelastic deflections of the twin tail. For the fluid flow, the initial conditions correspond to the freestream conditions with no-slip and no-penetration conditions on the wing and tail. For the aeroelastic deflections of the tail, the initial conditions for any point on the tail are that the displacement and velocity are zero, $w(z, 0) = 0$, $(\partial w/\partial t)(z, 0) = 0$, $\theta(z, 0) = 0$ and $(\partial\theta/\partial t)(z, 0) = 0$.

3. MULTI-DISCIPLINARY SOLUTION METHODOLOGY

This multi-disciplinary problem is solved using two steps. The first step is to solve for the fluid flow and the vortex breakdown flow around the rigid configuration. The initial condition of this step is the undisturbed freestream state. Navier–Stokes equations are then solved using the implicit, flux-difference splitting finite-volume scheme. The grid speed $\partial\xi^m/\partial t$ is set equal to zero in this step. In the second step, the vertical tails are assumed flexible and the configuration model is allowed to oscillate in rolling motion. The second step solves for the flow field around the configuration model and solves for the structural responses of the vertical tails. The initial condition of this step is the final solution of the first step. At every time step, the pressure differences across the tails are used to generate the normal force and twisting moment per unit length of each tail. Then, the aeroelastic equations are used to obtain the twin-tail deflections, $w_{i,j,k}$ and $\theta_{i,j,k}$. The grid displacement equations are then used to compute the new grid co-ordinates. The metric coefficients of the co-ordinate Jacobian matrix are updated as well as the grid speed, $\partial\xi^m/\partial t$. This computational cycle is repeated every time step. At each time step, the computational cycle consisting of the Navier–Stokes solver, the aeroelastic equations solver, and the grid displacement solver is repeated. Notice here that the rolling motion of the configuration is taken into account through the grid speed and grid displacements as well as the boundary conditions.

4. COMPUTATIONAL APPLICATIONS

4.1. TWIN-TAIL/DELTA-WING CONFIGURATION

The surface grid of the configuration model is shown in Figure 1. The configuration model consists of a 76°-swept back, sharp-edged delta wing of aspect ratio of one and dynamically scaled flexible twin tails similar to those used by Washburn *et al.* [6]. The vertical tails are oriented normal to the upper surface of the delta wing and have a leading-edge sweep of 62.5°. Each tail is modelled as a single aluminum spar hidden inside a balsa-wood covering, as shown in Figure 2. The aluminum spar has a taper ratio of 0·3 and a constant thickness of 1/32 of an inch. The root chord of the aluminum spar is 0·7 of an inch, and the tip chord is 0·2 of an inch. The span of the aluminum spar is 4 in long. The aluminum spar is constructed from 6061-T6 alloy with density, ρ, moduli of elasticity and rigidity, E and G, of 2693 kg/m^3, $6{\cdot}896 \times 10^{10}$ and $2{\cdot}5925 \times 10^{10}$ N/m^2 respectively. The

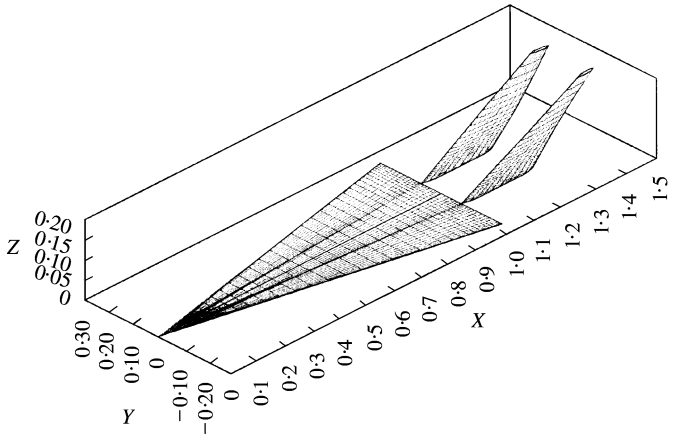

Figure 1. Surface grid of the delta-wing/twin-tail configuration model. The twin tails are in the inboard spanwise position.

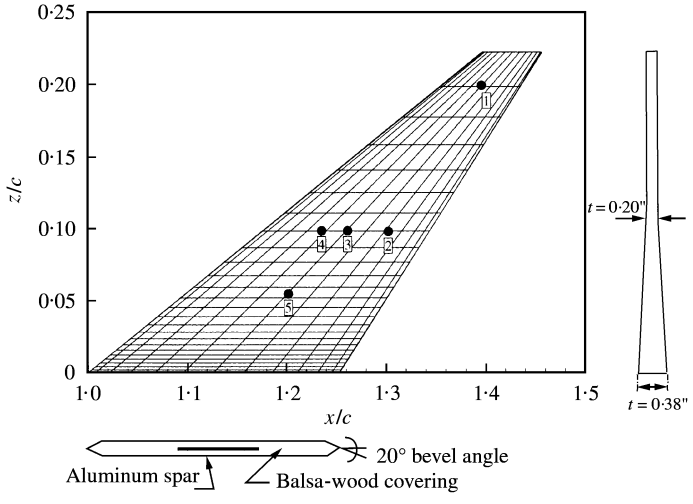

Figure 2. A schematic view of the tail construction and dimensions showing the pressure transducers locations: (1) 50% chord and 90% span; (2) 75% chord and 50% span; (3) 50% chord and 50% span; (4) 33% chord and 50% span; (5) 50% chord and 30% span.

corresponding dimensionless quantities are 2198, $4{\cdot}595 \times 10^5$ and $1{\cdot}727 \times 10^5$ respectively. The balsa-wood covering, which forms the wet surface of the vertical tail, has a taper ratio of 0·23 and an aspect ratio of 1·4. The root chord of the balsa-wood is 4·55 in, and the tip chord is 1·05 in. The span of the balsa-wood is 4 in long. The thickness of the balsa-wood decreases gradually from 0·38 of an inch at the tail root to 0·2 of an inch at the tail midspan. From the midspan to the tail tip, the thickness is kept constant and equals 0·2 of an inch. The tail cross-section has a semi-diamond shape with a bevel angle of 20°. The balsa-wood density, moduli of elasticity and rigidity are 179·7 kg/m^3, $6{\cdot}896 \times 10^8$ and $2{\cdot}5925 \times 10^8$ N/m^2 respectively. The corresponding dimensionless quantities are 147, $4{\cdot}595 \times 10^3$ and $1{\cdot}727 \times 10^3$ respectively. The fundamental bending and torsional frequencies of the tails are 33 and 307 Hz respectively. The non-dimensional fundamental bending and torsional frequencies are corresponding to $n = 0{\cdot}07$ and 0·65 respectively. Five pressure transducers, similar to those used by Washburn *et al.* [6], are used to monitor the unsteady pressure across the vertical tails, see Figure 2. The tails are assumed to be magnetically suspended and the leading edge of the tail root is positioned at the trailing edge of the delta wing.

The computational grid used in this study is a multi-block grid structure consisting of four blocks, C° continuous, with a total size of 465 250 grid points. The global grid extends 0·80 chord upstream, 3 chords radially and 3·5 chords downstream. The first block is an O–H grid covering the wing upstream region and the wing region up to the wing trailing edge, with $101 \times 50 \times 54$ grid points in the wrap around, normal and axial directions respectively. The second block is an H–H grid covering the inboard space between the twin tails, with $15 \times 50 \times 13$ grid points in the wrap around, normal and axial directions respectively. The third block is an H–H grid covering the outboard space between the twin tails, with $87 \times 50 \times 13$ grid points in the wrap around, normal and axial directions respectively. The fourth block is an O–H grid covering the downstream region of the twin tails, with $101 \times 50 \times 25$ grid points in the wrap around, normal and axial directions respectively. The three-dimensional grid topology and front view blow-up of the twin-tail/delta-wing configuration are shown in Figure 3.

The delta-wing/twin-tail configuration is statically pitched at 30° angle of attack and zero roll angle ($\theta_\circ = 0{\cdot}0$). The configuration is then forced to oscillate in roll around the symmetry axis at a constant amplitude of $\theta_a = 4^\circ$ and a reduced frequency ($K = \Omega \times c/a_\infty$)

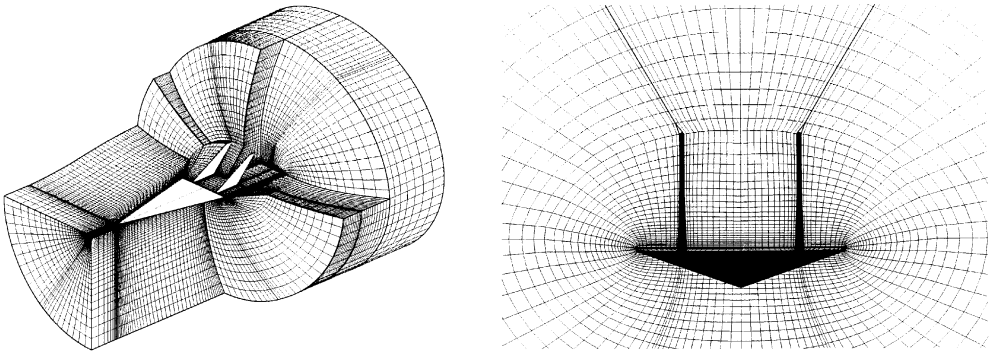

(a) (b)

Figure 3. (a) Three-dimensional view of the grid topology and (b) blow-up front view of the delta-wing/twin-tail configuration model. The twin tails are in the midspan position.

of either π or 2π. The forced rolling function is given by

$$\theta = \theta_0 + \theta_a \sin(K\tau). \tag{14}$$

The period of each cycle of oscillations corresponds to two or one dimensionless time respectively. Each cycle of oscillations requires 2000 or 1000 time steps, respectively, with a constant time-step of $\Delta t = 0{\cdot}001$. The motion starts with the right side of the wing (looking upstream) rolling in the counter-clockwise direction. The freestream Mach number and Reynolds number are 0·3 and $1{\cdot}25 \times 10^6$ respectively. The configuration is investigated for the inboard position of the twin tails, which corresponds to a separation distance between the twin tails of 33% of the wing span.

5. RESULTS AND DISCUSSION

5.1. CODE VALIDATION

The results of the present multi-disciplinary simulation tool have been validated using the experimental data of Washburn *et al.* [6]. The variations of the first two dominant non-dimensional frequencies against the angle of attack are shown in Figure 4. The results are shown for the inboard and outboard spanwise positions of the twin tails respectively. The experimental data of Washburn *et al.* [6] are also shown in the figure. In this figure, the frequencies are normalized by the freestream velocity and the tail span, where $n = 0{\cdot}74$ K. The tail span is used for frequency normalization rather than the wing chord in order to be consistent with the published experimental data. The results were in good agreement with the experimental data. At high angles of attack, the frequency peaks shift to a lower frequency. However, the peak frequencies observed for the inboard tail position vary less over the angle of attack range, compared to the case of outboard tails. The first two frequency peaks are moderately close to each other, which indicate that the pressure field contains energy over a narrow frequency band. This is in agreement with the observations of Martin and Thompson [16]. Detailed validation of the present multi-disciplinary simulation tool is presented by Sheta [15].

5.2. FLOW-FIELD RESULTS OF THE NO-ROLLING CASE

Snapshots of the flow-field around the flexible configuration model are shown in Figures 5–7. In these figures, the twin tails are allowed to move only due to the buffet loads.

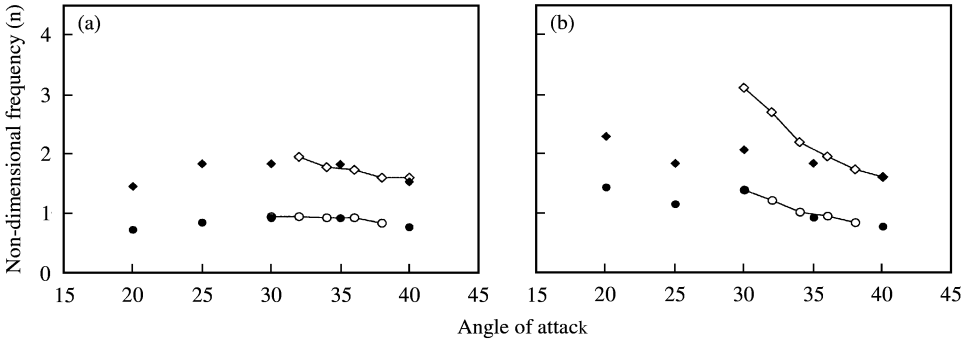

Figure 4. Non-dimensional predominant frequencies of the buffet excitation, compared with the experimental data of Washburn *et al.* [6]: (a) inboard twin-tail positions; (b) outboard twin-tail positions: —◇—, n_1 reference [6]; —○—, n_2 reference [6]; ◆, n_1 (CFD); ●, n_2 (CFD).

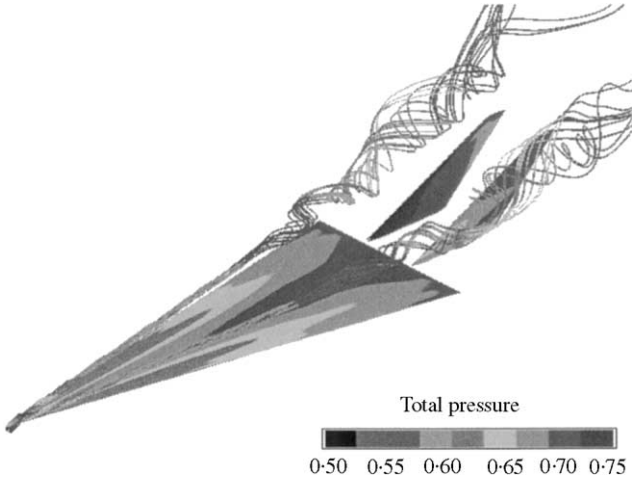

Figure 5. Three-dimensional snapshot view of the vortex-core instantaneous streamlines; stationary configuration with flexible tails.

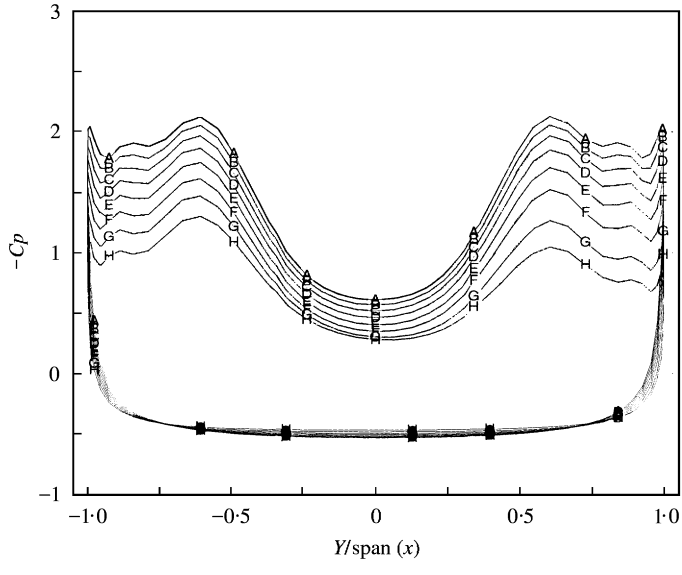

Figure 6. Distribution of coefficient of pressure on the upper and lower surfaces of the stationary configuration at different chord stations: A, $x/c = 0{\cdot}3$; B, $x/c = 0{\cdot}4$; C, $x/c = 0{\cdot}5$; D, $x/c = 0{\cdot}6$; E, $x/c = 0{\cdot}7$; F, $x/c = 0{\cdot}8$; G, $x/c = 0{\cdot}9$; H, $x/c = 1{\cdot}0$.

Figure 5 shows a three-dimensional view of the vortex-core instantaneous streamlines and the breakdown of the leading-edge vortices. The breakdown flow is asymmetric due to the irregular motion of the left and right vortices. The spanwise distribution of the surface pressure coefficient over the wing upper and lower surfaces at different chord stations is shown in Figure 6. Two suction pressure peaks are shown on the spanwise pressure distribution, corresponding to the wing primary and secondary vortices. Figure 7 shows total pressure contours and instantaneous streamlines on a cross-flow plane, intersecting the tails at $x/c = 1{\cdot}096$. The wing vortices are observed to be totally outboard of the twin tails. Smaller size vortex-cores appear under the vortex breakdown flows and at the lower

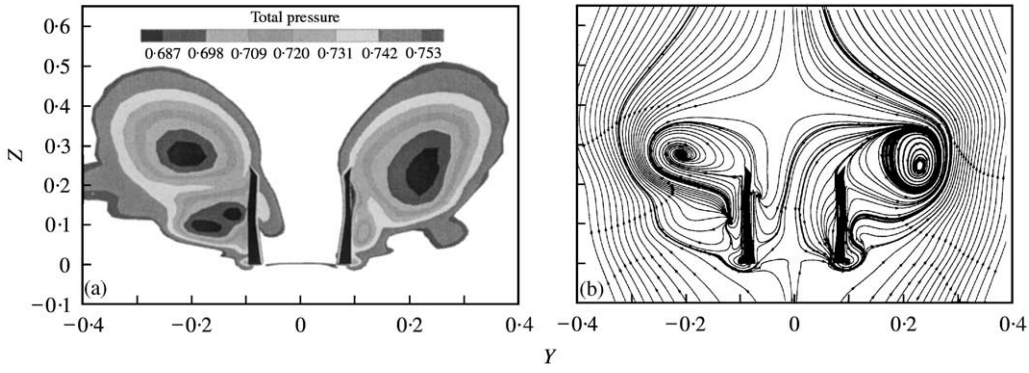

Figure 7. Snapshots on cross-flow plane, $x/c = 1{\cdot}096$. Stationary configuration with flexible tails: (a) total pressure, (b) instantaneous streamlines.

edges of the twin tails. These are the tail vortices observed experimentally by Washburn *et al.* [6]. The tail vortices exist totally at the outer surfaces of the tails and they are rotating in the opposite direction to those of the primary wing vortices.

5.3. EFFECT OF THE ROLLING OSCILLATIONS ON THE FLOW FIELD

In this section, the configuration model is forced to oscillate in rolling motion and the vertical tails are assumed flexible. For the case of rolling motion of reduced frequency of 2π, snapshots of the flowfield are given in Figures 8–10, every quarter of a cycle, during the eighth cycle of the rolling motion. Figure 8 shows the spanwise distribution of the surface pressure coefficient over the wing upper and lower surfaces at different chord stations. Figure 9 shows snapshots of the total pressure contours and instantaneous streamlines on a cross-flow plane ($x/c = 1{\cdot}096$). The snapshots clearly show the strengthening and weakening of the leading-edge vortices as the wing is rolling. At the beginning of a new cycle ($\theta = 0^\circ$), when the wing is rolling counterclockwise (looking upstream) and during half a cycle, the right leading-edge vortex becomes stronger than the left leading-edge vortex producing larger suction peaks over the right side of the wing. The pressure gradient across the right leading-edge vortex is also larger than that across the left leading-edge vortex. At the end of the second quarter ($\theta = 0^\circ$), when the wing is at zero roll angle and is moving in the CW direction, the right-vortex strength reaches its maximum, producing the highest suction peaks during the whole cycle. The left-vortex core is slightly more upward than that of the right vortex, during this half of the cycle. The right-tail vortex is also stronger than the left-tail vortex. At the end of the third quarter ($\theta = -4^\circ$), when the wing starts to roll in the CCW direction, the left leading-edge vortex becomes stronger than the right leading-edge vortex. The right-vortex core is now more upward than that of the left-vortex. Portions of the leading-edge vortices are shown in the inboard space between the twin tails, in contrast to the case of the stationary configuration.

Snapshots of the surface flow on the inner and outer surfaces of the right tail at the end of each quarter-cycle are shown in Figure 10. Starting from the end of the third quarter ($\theta = -4^\circ$) and during the next half-cycle, when the wing is rolling in the CCW direction, the leading-edge vortex separation and attachment lines on the right tail are moving upstream. During the second half of the cycle, when the wing is rolling in the CW direction, the separation and attachment lines are moving downstream. The attachment line of the tail

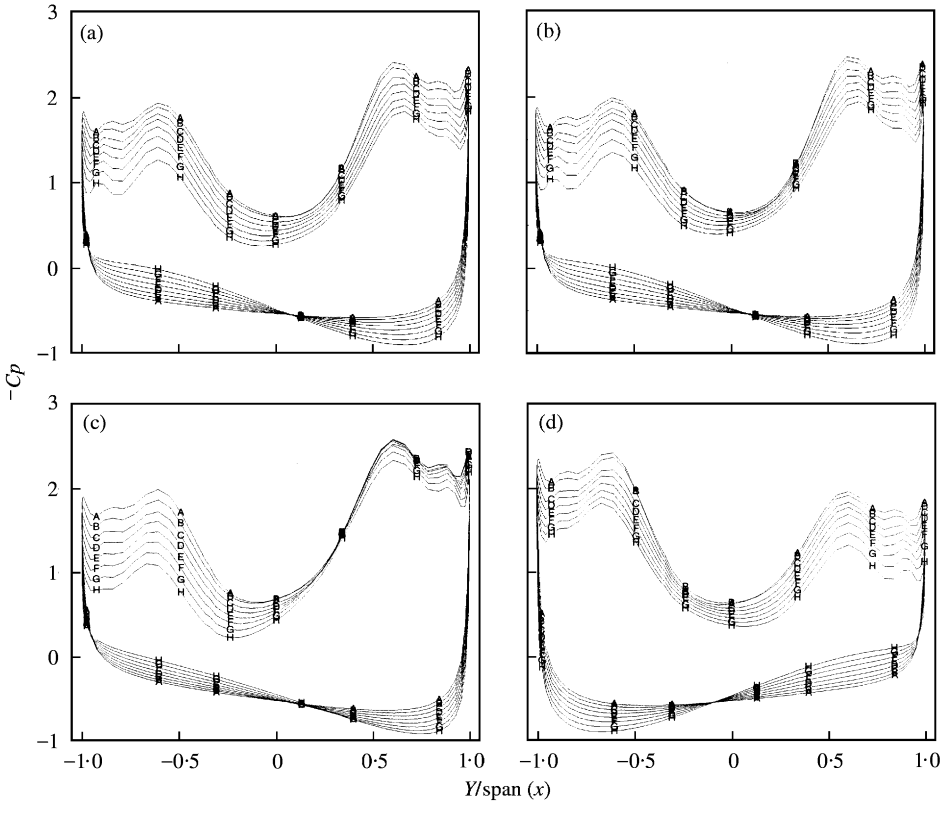

Figure 8. Distribution of coefficient of pressure on the wing upper and lower surfaces. Rolling motion, reduced frequency = 2π, flexible twin tails: (a) $\theta = 0^\circ$ moving CCW; (b) $\theta = 4^\circ$ moving CW; (c) $\theta = 0^\circ$ moving CW; (d) $\theta = -4^\circ$ moving CCW; A, $x/c = 0{\cdot}3$; B, $x/c = 0{\cdot}4$; C, $x/c = 0{\cdot}5$; D, $x/c = 0{\cdot}6$; E, $x/c = 0{\cdot}7$; F, $x/c = 0{\cdot}8$; G, $x/c = 0{\cdot}9$; H, $x/c = 1{\cdot}0$.

vortex appears parallel to the tail root, in agreement with the experimental observations of Washburn *et al.* [6].

The histories of the unsteady aerodynamic loads versus the non-dimensional time, and the instantaneous roll angle, θ, are shown in Figure 11. It is observed that the unsteady aerodynamic loads are oscillatory with the roll angle. This is attributed to the strengthening and weakening of the leading-edge vortices due to the rolling motion of the configuration model. The aerodynamic loads have never reached a complete periodicity. The coefficient of rolling moment is periodic only in the first three cycles. In a separate study by Menzies [17], a complete periodicity of the unsteady loads has been achieved for the rigid configuration at the same reduced frequency. Therefore, it is obvious that the unsteady loads lost the periodicity due to the irregular deflection motion of the left and right tails, which in turn affects the vortical flow over the wing. The coefficient of rolling moment oscillates in the range of $\pm 0{\cdot}7$. For the case of rolling at π reduced frequency, this range is $\pm 0{\cdot}06$. For comparison, the coefficient of rolling moment is of order 10^{-5} for stationary configuration.

5.4. TWIN-TAIL AEROELASTIC RESULTS

The aeroelastic results of the twin-tail buffet loading and response for uncoupled bending and torsion modes, $x_\theta = 0{\cdot}0$, are shown in Figures 12–19. Figure 12 shows the variation

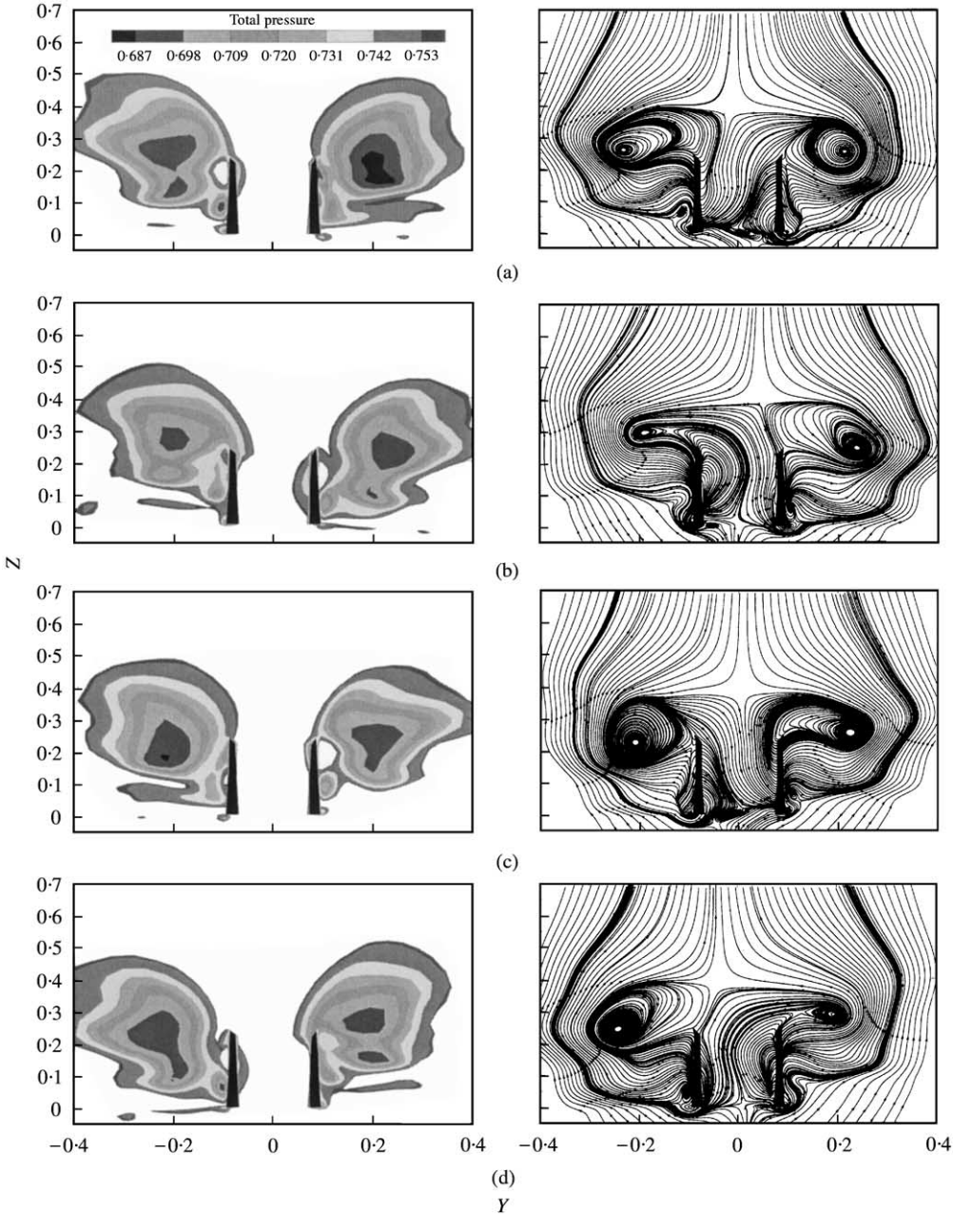

Figure 9. Snapshots of the total pressure contours (left) and the instantaneous streamlines (right) on cross-flow plane, $x/c = 1{\cdot}096$. Rolling motion, reduced frequency $= 2\pi$, flexible twin tails: (a) $\theta = 0^\circ$ moving CCW; (b) $\theta = 4^\circ$ moving CW; (c) $\theta = 0^\circ$ moving CW; (d) $\theta = -4^\circ$ moving CCW.

of the normal force and twisting moment coefficients, of the stationary configuration, along the tail span every two dimensionless time units for the left and right tails. The variation of the load distribution at different time levels shows the unsteady characteristics of the loads over the tails. It is observed that while the maximum normal forces are at the tail root, the maximum twisting moments are almost at the 20% station of the tail span. Figure 13

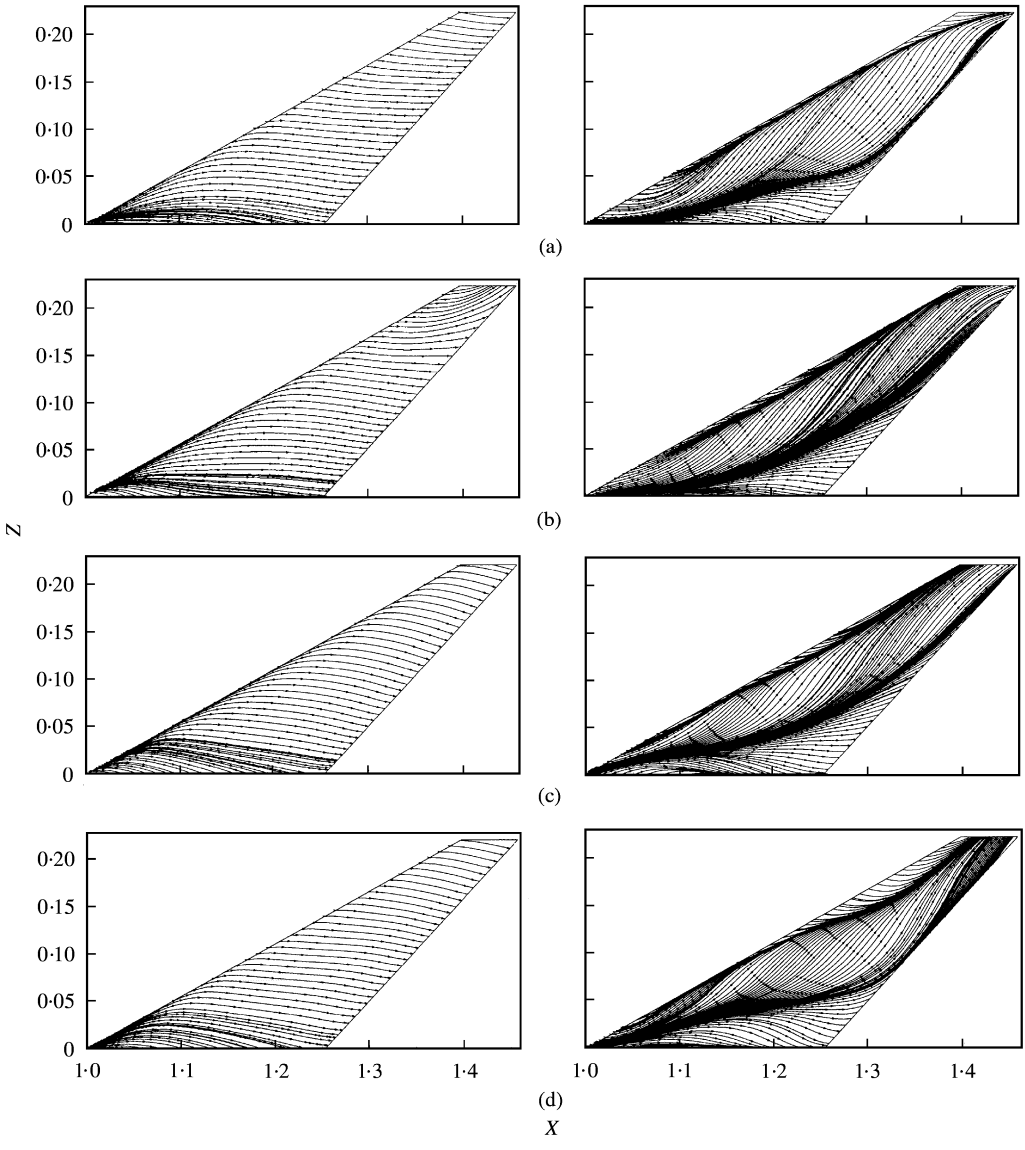

Figure 10. Surface flow on the inner surface (left) and the outer surface (right) of the right tail. Rolling motion, reduced frequency $= 2\pi$, flexible twin tails: (a) $\theta = 0^\circ$ moving CCW; (b) $\theta = 4^\circ$ moving CW; (c) $\theta = 0^\circ$ moving CW; (d) $\theta = -4^\circ$ moving CCW.

shows the mean and r.m.s. distribution of the normal force and twisting moment coefficients along the tail span. The mean values are slightly decreased with the increase of the reduced frequency; however, the r.m.s. values are increased with the increase of the reduced frequency. Figures 14 and 15 show the time and frequency domains of the tail-root bending moment and twisting moment coefficients respectively. It is obvious that the rolling oscillations have produced larger loads and frequency of loads than those of the stationary configuration. The PSD peaks of the root bending moment and root twisting moment are increased with the increase of the reduced frequency. However, the predominant moments peaks have shifted to a higher frequency for the rolling case at 2π reduced frequency.

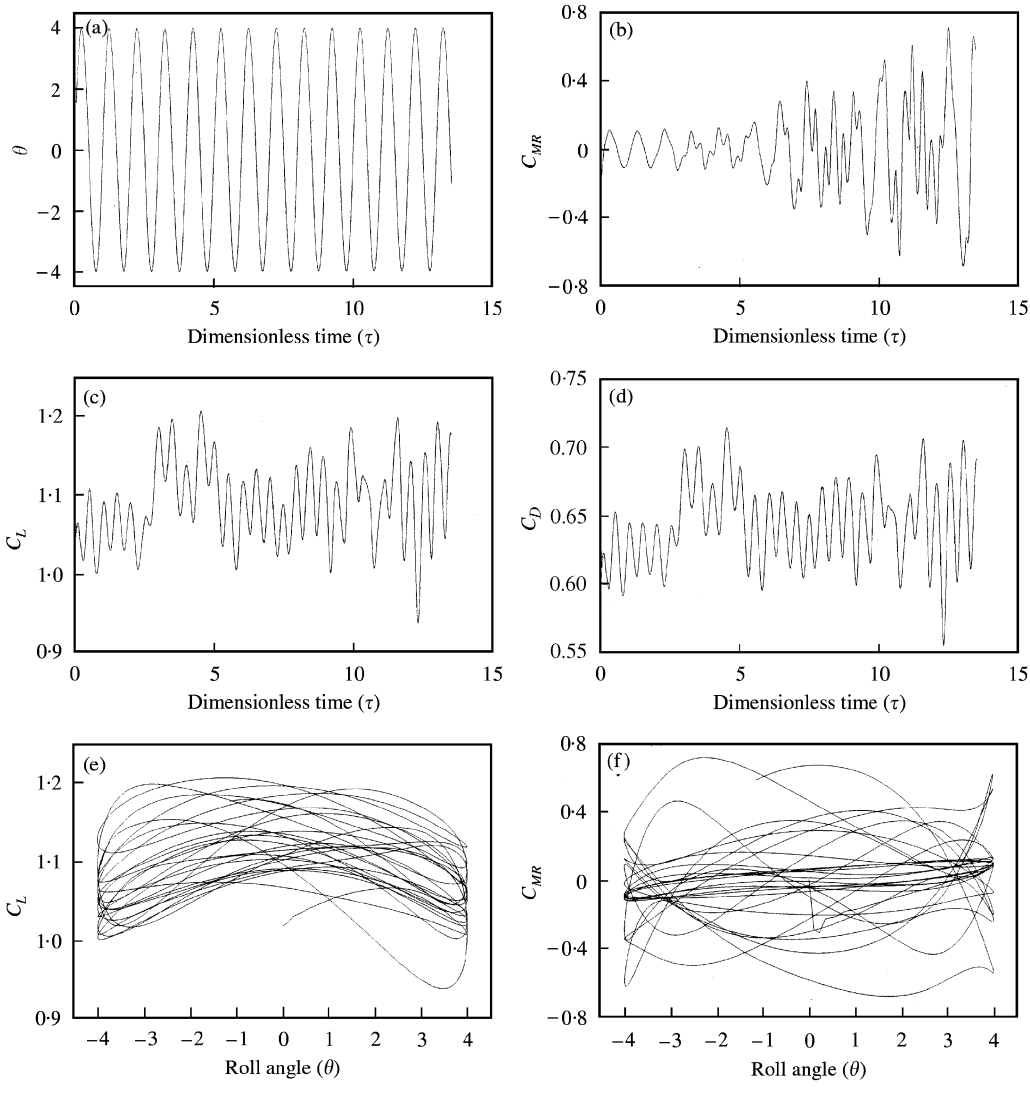

Figure 11. Unsteady aerodynamic loads coefficients of the configuration model in rolling motion, reduced frequency = 2π. Delta wing with flexible twin tails. (a) Roll angle, (b) coefficient of rolling moment, (c) coefficient of lift, (d) coefficient of drag, (e) coefficient of lift, (f) coefficient or rolling moment.

Figure 16 shows the variation of the bending deflection, w, and torsion deflection, θ, of the stationary configuration, along the tail span every two dimensionless time units for the left and right tails. The tail deflections are in the first and second mode shapes. The two tails are moving opposite to each other but in an asymmetric manner. Figure 17 shows the time histories of the tail-tip bending deflection, torsion deflection, bending acceleration and torsion acceleration, for the left and right tails. Figure 18 shows the frequency domain of the tail-tip bending and torsion accelerations. The rolling oscillations produced higher bending deflection and acceleration. However, the amplitude of bending deflection and acceleration are higher for the case of reduced frequency of π than at higher reduced frequency. The torsion deflection and acceleration for the 2π reduced frequency case are less than those of the stationary configuration. However, in the π reduced frequency case, they are higher than

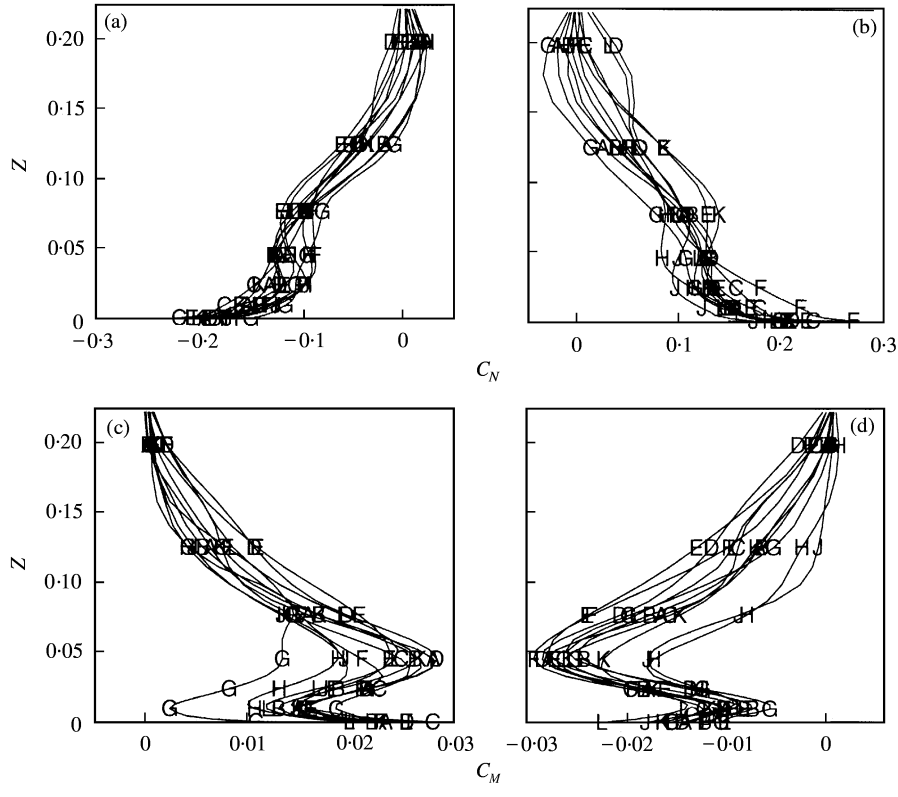

Figure 12. Distribution of the normal forces and twisting moments coefficients along the span of the flexible twin tails: (a) C_N of left tail; (b) C_N of right tail; (c) C_M of left tail; (d) C_M of right tail: A, $\tau = 0{\cdot}0$; B, $\tau = 2{\cdot}0$; C, $\tau = 4{\cdot}0$; D, $\tau = 6{\cdot}0$; E, $\tau = 8{\cdot}0$; F, $\tau = 10$; G, $\tau = 12$; H, $\tau = 14$; J, $\tau = 16$; K, $\tau = 18$; L, $\tau = 20$.

both the static configuration case and the 2π reduced frequency case. The *PSD* of the right-tail-tip bending and torsion accelerations are maximum at π reduced frequency case. Figure 19 shows the buffet excitation spectra on both sides of the right tail at the near-tip pressure transducer (50% chord and 90% span). The buffet excitation peaks are obviously increased with the increase of the reduced frequency.

Finally, the present multi-disciplinary analysis tool costs about 7·64 μs per grid cell per time step using a single processor of a Cray C-90 for the full Navier–Stokes equations. The total computational cost per 15 000 time steps case is about 15 h of CPU working time. Edwards [17] assessed the computational cost of direct numerical simulations of tail buffet of full-span F-15 aircraft by 40 μs per grid cell per time step using thin-layer Navier–Stokes equations. Therefore, it is believed that the present multi-disciplinary analysis tool is a fast tool for the prediction and control of the buffet phenomenon of fighter aircraft.

6. CONCLUSION

The effect of dynamic rolling oscillations of delta-wing/twin-tail configuration on twin-tail buffet response is investigated. The problem is investigated for the inboard position of the twin tail which corresponds to a separation distance between the twin tail of

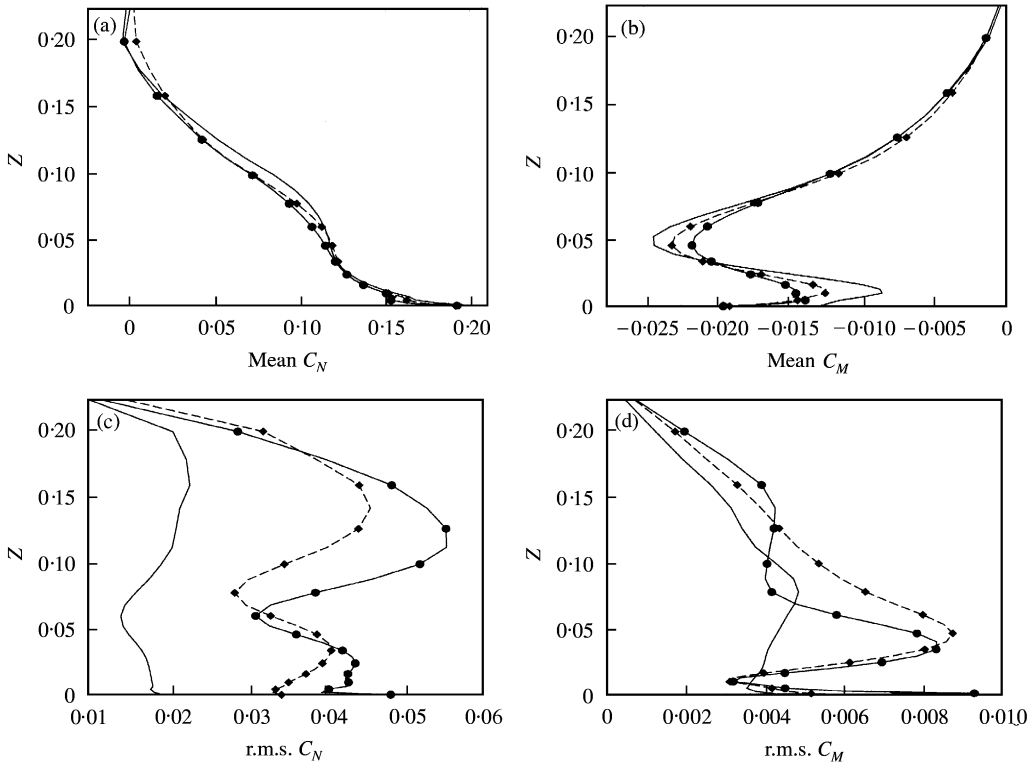

Figure 13. Effect of the reduced frequency of the rolling motion on the distribution of the normal forces and twisting moments along the tail span of the flexible right tail: (a) mean normal forces; (b) mean twisting moments; (c) r.m.s. normal forces; (d) r.m.s. twisting moments: ——, $K = 0{\cdot}0$; – – ◆ – –, $K = \pi$; —●—, $K = 2\pi$.

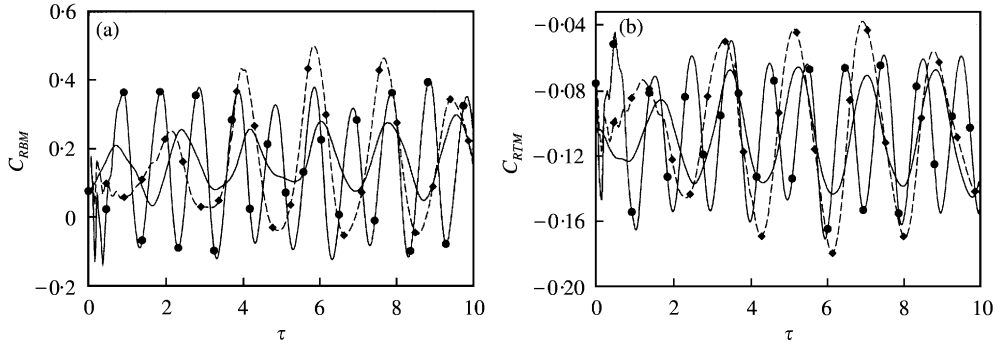

Figure 14. Effect of the reduced frequency of the rolling motion on the history of the right flexible tail root moment coefficients: (a) root bending moment; (b) root twisting moment; ——, $K = 0{\cdot}0$; – – ◆ – –, $K = \pi$; —●—, $K = 2\pi$.

33% wing chord. The configuration model is statically pitched to 30° angle of attack and then forced to oscillate in roll around the symmetry axis by a constant amplitude of 4° and reduced frequency of π and 2π. The unsteady aerodynamic loads have never reached complete periodicity due to the irregular vibrations of the left and right tails. The buffet loads, responses, and the excitation peaks were higher than those of stationary

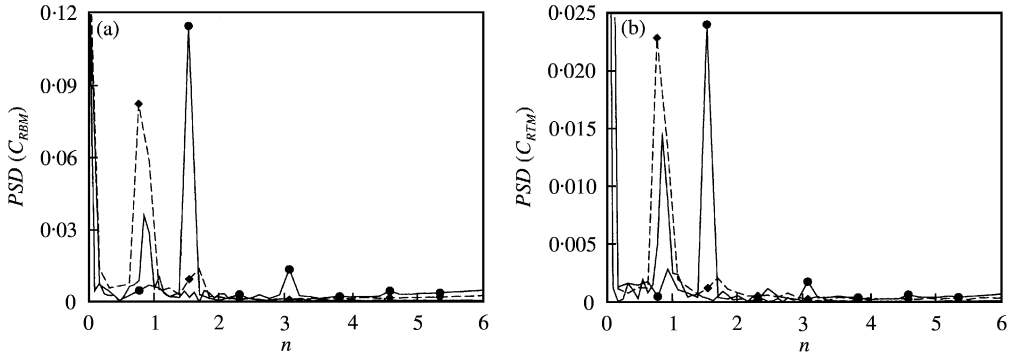

Figure 15. Effect of the reduced frequency of the rolling motion on the power spectral density of the right flexible tail root moment coefficients: (a) PSD of root bending moment; (b) PSD of root twisting moment; ——, $K = 0{\cdot}0$; – – ◆ – –, $K = \pi$; —●—, $K = 2\pi$.

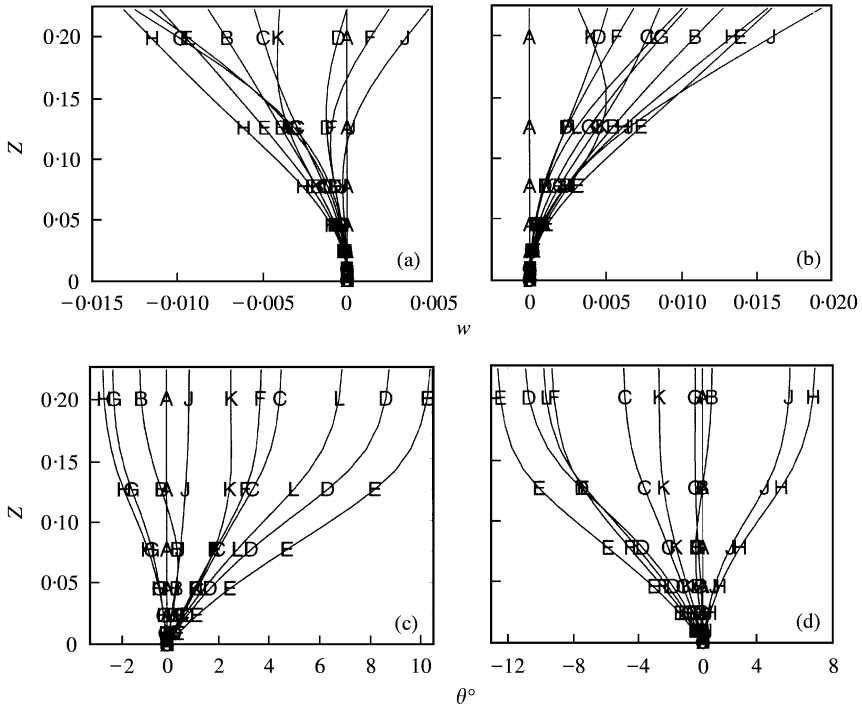

Figure 16. Distribution of the bending and torsional deflections along the span of the flexible twin tails: (a) bending deflection of left tail, (b) bending deflection of right tail, (c) torsional deflection of left tail, (d) torsional deflection of right tail, A, $\tau = 0{\cdot}0$; B, $\tau = 2{\cdot}0$; C, $\tau = 4{\cdot}0$; D, $\tau = 6{\cdot}0$; E, $\tau = 8{\cdot}0$; F, $\tau = 10$; G, $\tau = 12$; H, $\tau = 14$; J, $\tau = 16$; K, $\tau = 18$; L, $\tau = 20$.

configurations. This indicated that the buffet phenomenon is even worse during the dynamic maneuvers of fighter aircraft. Increasing the reduced frequency has led to higher buffet loads, higher frequencies of loads, and higher excitation peaks in the loads spectra. However, it has also lead to lower bending and torsion deflections and accelerations than those at lower reduced frequency.

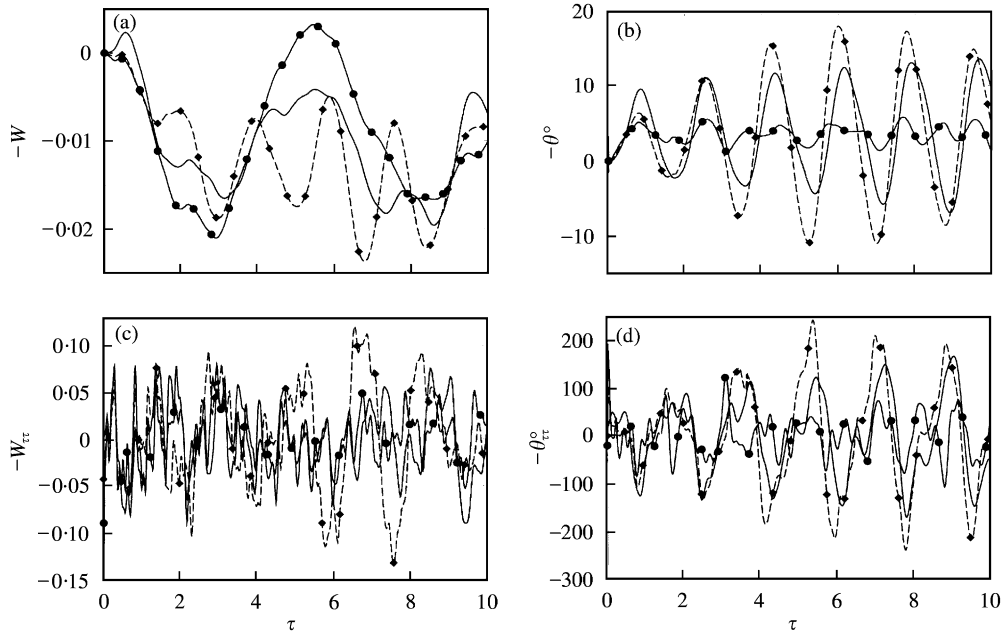

Figure 17. Effect of the reduced frequency of the rolling motion on the history of the deflections and accelerations of the tail tip of the right flexible tail: (a) bending deflection, (b) torsional deflection, (c) bending acceleration, (d) torsional acceleration; ——, $K = 0{\cdot}0$; – – ◆ – –, $K = \pi$; —●—, $K = 2\pi$.

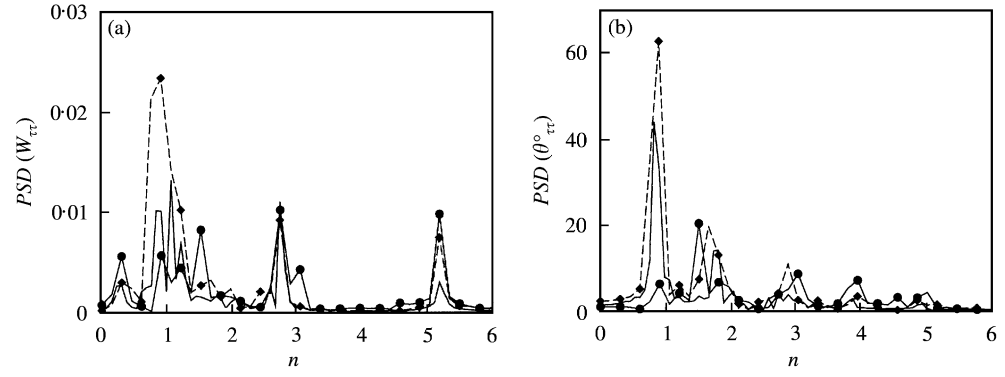

Figure 18. Effect of the reduced frequency of the rolling motion on the power spectral density of the bending and torsional accelerations of the tail tip of the right flexible tail: (a) PSD of bending acceleration, (b) PSD of torsional acceleration; ——, $K = 0{\cdot}0$; – – ◆ – –, $K = \pi$; —●—, $K = 2\pi$.

ACKNOWLEDGMENTS

This research work is supported by the Aeroelasticity Branch of NASA Langley Research Center, under Grant No. NAG-1-648. The authors would like to acknowledge the computational resources provided by the NAS facilities at NASA Ames Research Center and NASA Langley Research Center (LaRC).

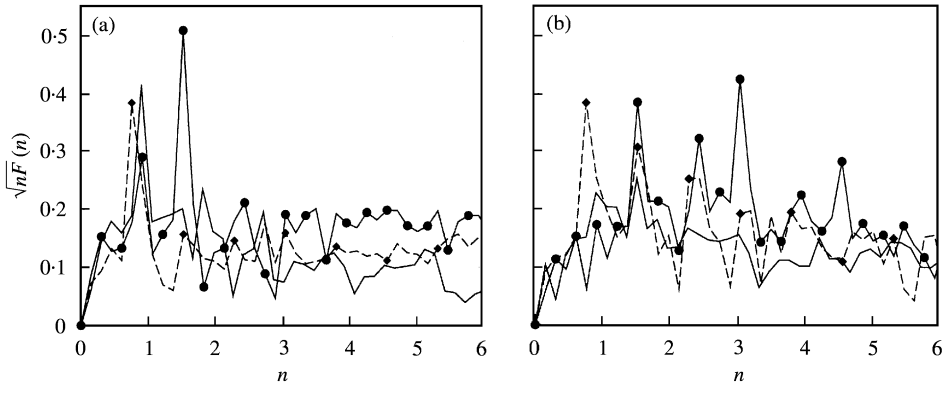

Figure 19. Effect of the reduced frequency of the rolling motion on the buffet excitation spectra of the right tail tip transducer, 50% chord and 90% span: ——, $K = 0{\cdot}0$; – –◆– –, $K = \pi$; —●—, $K = 2\pi$.

REFERENCES

1. W. L. Sellers III, J. F. Meyers and T. E. Hepner 1988 *SAE Paper* 88-1448. LDV survey over a fighter model at moderate to high angle of attack.
2. G. E. Erickson, R. M. Hall, D. W. Banks, J. H. Del Frate, J. A. Shreiner, R. J. Hanley and C. T. Pulley 1989 *AIAA Paper* 89-2222. Experimental investigation of the F/A-18 vortex flows at subsonic through transonic speeds.
3. W. H. Wentz 1987 *AIAA Paper* 87-2474. Vortex–fin interaction on a fighter aircraft.
4. B. Lee and D. Brown 1990 *AIAA Paper* 90-1432. Wind tunnel studies of F/A-18 tail buffet.
5. S. R. Cole, S. W. Moss and R. V. Dogget Jr 1990 *NASA TM*-102749. Some buffet response characteristics of a twin-vertical-tail configuration.
6. A. E. Washburn, L. N. Jenkins and M. A. Ferman 1993 *AIAA Paper* 93-0050. Experimental investigation of vortex–fin interaction.
7. O. A. Kandil, H. A. Kandil and S. J. Massey 1993 *AIAA Paper* 93-3688-*CP*. Simulation of tail buffet using delta wing-vertical tail configuration.
8. O. A. Kandil, S. J. Massey and H. A. Kandil 1994 *AIAA Paper* 94-1428-*CP*. Computations of vortex-breakdown induced tail buffet undergoing bending and torsional vibrations.
9. O. A. Kandil, S. J. Massey and E. F. Sheta 1996 *Journal of Royal Aeronautical Society* 297–303. International Forum on Aeroelasticity and Structural Dynamics. Structural dynamics/CFD interaction for computation of vertical tail buffet.
10. O. A. Kandil, E. F. Sheta and S. J. Massey 1995 *AIAA Paper* 95-3464-*CP*. Buffet responses of a vertical tail in vortex breakdown flows.
11. O. A. Kandil, E. F. Sheta and S. J. Massey 1996 *AIAA Paper* 96-2517-*CP*. Twin tail/delta wing configuration buffet due to unsteady vortex breakdown flow.
12. O. A. Kandil, S. J. Massey and E. F. Sheta 1996 *High-Angle-of-Attack Technology Conference, NASA Langley Research Center, Hampton, VA*. Aerostructural vortical flow interactions with applications to F/A-18 and F-117 tail buffet.
13. O. A. Kandil, E. F. Sheta and S. J. Massey 1997 *AIAA Paper* 97-2261-*CP*. Fluid/structure twin tail buffet response over a wide range of angles of attack.
14. E. F. Sheta and O. A. Kandil 1988 *AIAA Paper* 98-0520. Effect of configuration pitching motion on twin tail buffet response.
15. E. F. Sheta 1998 *Ph.D. Dissertation, Old Dominion University*. Computational investigation and validation of twin-tail buffet response including dynamics and control.
16. C. A. Martin and D. H. Thompson 1991 *AGARD-CP*-497. Scale model measurements of fin buffet due to vortex bursting on F/A-18.
17. M. A. Menzies 1995 *Ph.D. Dissertation, Old Dominion University*. Unsteady, transonic flow around delta wings undergoing coupled and natural modes response—a multidisciplinary problem.
18. J. W. Edwards 1990 *NASA TM* 101613. Assessment of computational prediction of tail buffeting.

APPENDIX A: NOMENCLATURE

a_∞	speed of sound of freestream
b	vertical-tail span
c	root chord of delta wing
C_M	twisting moment coefficient
C_N	normal force coefficient
E	elastic modulus of elasticity
f	frequency (Hz)
G	elastic modulus of rigidity
$I(z)$	area moment of inertia
I_θ	mass moment of inertia about the elastic axis
$J(z)$	geometrical torsional constant
K	reduced frequency of rolling ($=\Omega \times c/a_\infty$)
$[K]$	structural stiffness matrix
$[M]$	structural mass matrix
n	non-dimensional frequency ($=f \times b/U_\infty$)
$N(z, t)$	normal force per unit length
$m(z)$	tail cross-section mass per unit length
M	Mach number
$M(z, t)$	torsional moment per unit length
U_∞	freestream velocity
x_∞	distance between the elastic axis and the inertial axis
w	bending deflection of the tail
θ	torsional deflection angle, rad
ϕ	free vibration modes
α, (AOA)	angle of attack
Ω	angular velocity vector